Supporting information

Highly Ordered Ultrathin Perfluorinated Sulfonic Acid Ionomer Membranes for Vanadium Redox Flow Battery

Jongmin Q. Kim,[a,b] *Soonyong So,*[c,*] *Hee-Tak Kim,*[a,b] *Siyoung Q. Choi*[a,b,*]

[a]Department of Chemical and Biomolecular Engineering, Korea Advanced Institute of Science and Technology (KAIST), Daejeon 34141, South Korea

[b]Advanced Battery Center, KAIST Institute for the NanoCentury, KAIST, Daejeon 34141, South Korea

[c]Energy Materials Research Center, Korea Research Institute of Chemical Technology (KRICT), Daejeon 34114, South Korea

AUTHOR INFORMATION

Corresponding Authors

*Soonyong So - E-mail: syso@krict.re.kr

*Siyoung Q. Choi - E-mail: sqchoi@kaist.ac.kr

1. Experimental Section

Materials: The ultrathin PFSA membranes in this work were fabricated with 5 wt% PFSA dispersion solution (Nafion™ D520 dispersion, equivalent weight: 1000 g/mol of SO_3H) purchased from DuPont (USA). The pH 2 aqueous solution was prepared using hydrochloric acid (37%, Sigma-Aldrich, USA) and ultrapure deionized (DI) water (18.2 MΩ·cm, Merck-Millipore, USA). A 47 mm diameter Whatman® Nuclepore track-etched polycarbonate (PC) membrane (50 nm pore diameter, 111103, GE Healthcare Biosciences, USA) was used as a porous support.

Formation of the PFSA monolayer at the air/water interface: The ultrathin PFSA membranes on a porous support were prepared by forming and condensing the PFSA monolayer on the air/water interface using a Langmuir trough (KN2002, KSV NiMA, Biolin Scientific, Finland). The surface pressure was measured by using a Wilhelmy plate. In order to make a more homogeneous and compressed monolayer, a separate addition method was used utilizing a total of 50 µL of 5 wt% D520 dispersion. In each separated step, 10 µL of dispersion was spread onto 165 mL of pH 2 aqueous subphase interface using a micro-syringe (50 µL, Hamilton, USA). The floating PFSA monolayer was then compressed at a barrier speed of 27 mm/min to a surface pressure of 54 mN/m. After that, the decompression step was conducted with the same barrier rate. These spreading, compression, and decompression steps were repeated five times. After the PFSA monolayer was compressed at the barrier rate of 5 mm/min, and the compactly condensed PFSA monolayer was finally obtained on the air/water interface.

Deposition of the PFSA monolayers on the substrate: The PFSA monolayers on the air/water interface were transferred to the surface of the substrates using the Langmuir-Blodgett (LB)

deposition method (vertical dipping). This process was carried out with the substrate fixed to the dipper moving up and down at a dipper speed of 5 mm/min under the surface pressure of 54 mN/m. Si wafers hydrophobic treated with octadecyltrichlorosilane (OTS) were used as a substrate instead of PC membranes for multilayer characterizations with GISAXS. After the depositions steps, the fabricated samples were dried at 80 °C for 16 hours. The detailed procedure is explained in **Discussion S4** in the discussion section.

To compare the properties of the membrane with ultrathin PFSA monolayers, the casted Nafion (CN) was fabricated by dispersion-casting using 20 wt% PFSA dispersion solution (Nafion™ D2021 dispersion, equivalent weight: 1100 g/mol of SO_3H). After drying and annealing at 120 °C, CN was finally obtained with a thickness of 10 μm.

Grazing incidence small angle X-ray scattering (GISAXS) experiments: In order to evaluate the structure of the PFSA membrane stacked by the LB method, the GISAXS experiments were carried out at a beamline 3C at Pohang Accelerator Laboratory (PAL). Two-dimensional scattering patterns were collected at a grazing incidence angle (α) of 0.16 ° between the critical angles for the substrates and the thin films, and were recorded with a MAR CCD detector at room temperature. The X-ray beam wavelength (λ) was 1.23 Å and the sample-to-detector distance was 859 mm. The *d*-spacing values (d) between stacked PFSA membranes were calculated from scattering vectors q ($d = 2\pi/q$).

Surface pore analysis of PC50 and composite membranes: Analyses of surface morphologies and pores of composite membranes, were performed using a SEM (S-4800, Hitachi, USA). The

number of pores and their area at the surface of each membrane were analyzed from SEM images using *Image J* software (NIH).

Vanadium ion permeation test: The permeation tests of vanadium ion (VO^{2+}) were carried out using a home-made diffusion cell. The diffusion cell consisted of two chambers separated by the membrane with an effective area of 2.84 cm^2. One chamber was filled with 80 mL of 2 M $VOSO_4$ in 3 M H_2SO_4 and the other was filled with the same volume of 2 M $MgSO_4$ in 3 M H_2SO_4. Both chambers were continuously stirred at 40 °C to prevent crystallization of $MgSO_4$. The transient concentration of permeated VO^{2+} was measured using an UV-VIS spectrometer (Cary 8454 UV−Vis, Agilent Technologies, USA) at a maximum absorption peak at the wavelength of 760 nm. The VO^{2+} permeability (P) of the membrane was obtained using the following equation:

$$P\ [\mathrm{m^2/s}] = \frac{VL}{AC_0} \times \frac{dC}{dt}\ , \qquad \text{Equation S1}$$

where V is the solution volume (80 mL) in the chamber, L is the thickness of the membrane, A is the effective area (2.84 cm^2), C_0 is the initial concentration of vanadium ion in the solution (2 M), and dC/dt is the concentration change of vanadium ion by time in the $MgSO_4$ solution.

From the P of the membrane, the VO^{2+} permeance (p) of the membrane was evaluated using following **Equation S2**.

$$p\ [\mathrm{m/s}] = P/L\ . \qquad \text{Equation S2}$$

Area resistance, proton conductance, and proton conductivity of membrane: The electrical resistance of the membranes was measured using a multi-meter (3560 AC mΩ HiTESTER, HIOKI. Ltd., Japan). 1.5 M H_2SO_4 was used as the electrolyte, and the measurements were conducted at room temperature. The area resistance (R) of the membrane was calculated from the following equation:

$$R\ [\Omega\ \mathrm{cm}^2] = (r_2 - r_1) \times A\ , \qquad \text{Equation S3}$$

where r_2 and r_1 are the resistance with and without the membrane, respectively, and A is the effective area (0.196 cm^2).

From the resistance of the membrane, the proton conductance (κ) was estimated using **Equation S4**.

$$\kappa\ [\mathrm{S}] = A/R\ . \qquad \text{Equation S4}$$

The proton conductivity (σ) of the membrane was obtained from the area resistance of the membrane using the following equation:

$$\sigma\ [\mathrm{S/m}] = L/R\ . \qquad \text{Equation S5}$$

Ion selectivity: The ion selectivity of the membrane (S) was calculated using **Equation S6**:

$$S\ [\mathrm{S \cdot s/m^3}] = \sigma/P\ . \qquad \text{Equation S6}$$

Vanadium redox flow battery single cell test: For VRFB single cell testing, a dried membrane was sandwiched between two sets of copper current collectors, graphite bipolar plates, and carbon felt electrodes. The single cell was assembled carefully by tightening. The effective area was 2 × 2 cm^2, and 12 mL of V^{3+}/VO^{2+} (1.65 M, 1:1 mol/mol, Prudent Energy Inc.) in 3 M H_2SO_4 was used as a starting electrolyte for positive and negative electrolytes. Each electrolyte was cyclically pumped into half-cells at a rate of 20 mL/min. A VRFB single cell was operated by a battery cycler (Scribner Associates Inc., 857 redox cell test system) under the cutoff voltages for discharge and charge at 1.0 and 1.6 V, respectively. The rate performance of the VRFBs was carried out at various current densities between 40 and 200 mA/cm^2. CE (%) and EE (%) were evaluated by the ratio of capacity and energy of discharging-charging cycles, respectively, and VE (%) was calculated by VE = EE/CE × 100 (%).

The long-term cycling stability was conducted at a constant current density of 200 mA/cm^2 for 800 charge/discharge cycles. The open circuit voltage (OCV) test was performed after charging to 1.6 V for the self-discharge evaluation. The VRFB was kept at the open circuit until the voltage was lower than 0.8 V under the constant electrolyte circulation rate of 20 mL/ min.

2. Discussion Section

Discussion S1. Effect of equivalent weight (EW) and side chain length of PFSA ionomer to interfacial strength and ion transport properties of PFSA monolayer

Polymer monolayers on the air/water interface can be generally formed by two preparation methods: spontaneous adsorption of polymers to the interface from a bulk aqueous solution (Gibbs monolayers) and direct spreading of the polymer dispersion on the interface (Langmuir monolayers). In particular, because of irreversible adsorption on the air/water interface, PFSA ionomers can effectively form a Langmuir monolayer on the interface using a small amount of PFSA dispersion without dissolution into water even though the ionomers are dispersed in the aqueous solution.[1,2] The formation and stability of PFSA monolayer on the interface as well as the deposition of it onto the substrates are affected by interfacial properties of PFSA monolayer on the air/water interface. The rheological properties of PFSA monolayer mainly originated from the electrostatic interaction of SO_3^- groups of side chains of PFSA, not direct interaction between PTFE backbones. The rheological properties also depend on EW and the side chain length of PFSA.[3] PFSA ionomers with a higher EW tend to create stiffer monolayers on the interface due to high surface activity. In addition, as the PFSA ionomers have longer side chains, the monolayer at the interface shows the larger the shear modulus at the same surface pressure, presumably because the side chains form the better closed packing structure.

The ion conductivity of PFSA ionomers is also affected by EW. In contrast to the interfacial strength, PFSA ionomers with a lower EW (higher ion exchange capacity (IEC), IEC [mmol-SO_3H/g] = 1000/EW) show higher ion conductivity due to more expanded ionic clusters.[4,5] Considering the sufficient interfacial strength and ion conductivity, a PFSA of EW 1000 g/mol

of SO_3H (D520, 5 wt% in alcohol based solution) was used for fabrication of ultrathin PFSA ionomer membranes.

Discussion S2. Effect of subphase and surface pressure (Π) according to spreading amounts of PFSA ionomer solution

Π of the PFSA Langmuir monolayer depends on the subphase and spreading amounts. In general, electrolytes, such as NaCl, KCl, and HCl, stabilize SO_3^- groups of PFSA ionomers by charge screening, resulting in enhanced polymer adsorption on the air/water interface.[6,7] In particular, HCl aqueous solution not only increases the efficiency of adsorption and stability of the monolayer on the interface, but also maintains the H^+-form of PFSA without cation exchange, which can alter PFSA properties.[8,9] Thus, a HCl aqueous solution of pH 2 was used as subphase in all of the preparation steps of the PFSA mono-LB layer.

As shown in **Figure S1**, Π of the PFSA Langmuir monolayer rapidly increases as the D520 solution was spread onto the air/HCl aqueous solution interface compared with pure water as a subphase. Π of both cases increase up to $\Pi \sim 43$ mN/m by absorbing PFSA ionomers on the interface. After the saturation point, the Π of the PFSA monolayer did not increase, even though more PFSA ionomers were loaded. When the HCl aqueous solution (pH 2) was utilized as a subphase, a smaller amount of PFSA ionomer was required for the maximum Π; only 10 μL of D520 for HCl aqueous solution, but 40 μL of D520 in case of water.

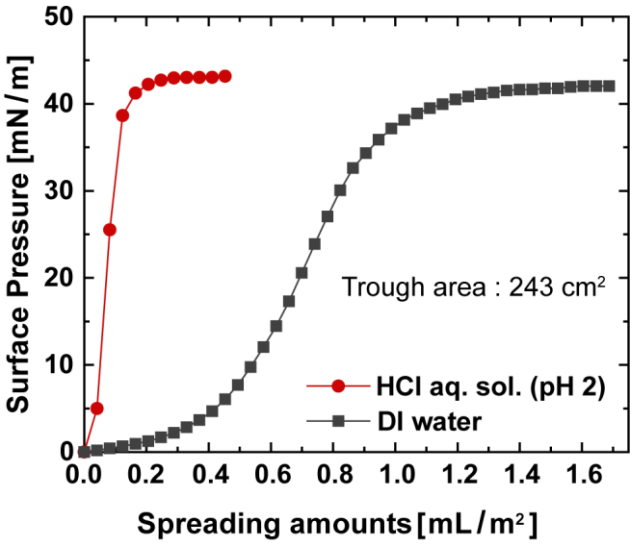

Figure S1. Surface pressure (Π) measurements of D520 Langmuir monolayer on the air/water interface formed in the 243 cm^2 of Langmuir trough. HCl aqueous solution (red circle) and water (black square) were used as a subphase. The D520 dispersion was spread onto the air/each subphase interface, respectively. As increasing spreading amounts on the interface, surface pressures increase in both subphases, and saturate at Π ~ 43 mN/m. However, when the HCl aqueous solution was the subphase, the spreading amount of the D520 dispersion is less than that of water until the saturation point. These indicate that PFSA ionomer fully occupied the trough area at Π ~ 43 mN/m and the adsorption efficiency of PFSA ionomers was higher on the HCl aqueous solution.

Discussion S3. PFSA monolayer behavior on the air/water interface by physical compression

The surface pressure-area (Π-A) isotherm of the PFSA Langmuir monolayer was obtained to investigate the monolayer behavior on the air/water interface (**Figure S2**). As the PFSA monolayer was physically compressed with the barrier speed of 5 mm/min, the ionomer molecules were closely packed to minimize the surface pressure, which results in a gradual increase of the surface pressure.[10] Above Π = 54 mN/m, collapse of the monolayer, which is irreversible out-of-plane deformation of the monolayer, occurred.[2]

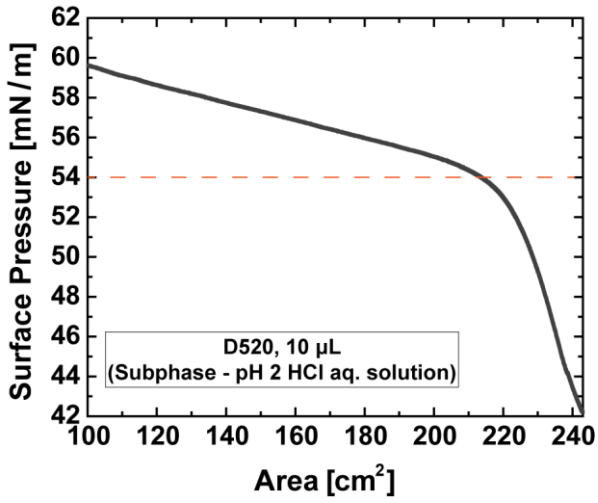

Figure S2. Surface pressure-area (*Π*-*A*) isotherm of PFSA Langmuir monolayer on the air/water interface. 10 µL of D520 dispersion was spread onto interface until *Π* reached 43 mN/m. At room temperature, the PFSA monolayer was compressed at a barrier speed of 5 mm/min. As the trough area decreases from 243 cm^2 (initial area) to 100 cm^2, *Π* gradually increases. Above *Π* = 54 mN/m, collapse of the PFSA monolayer was observed.

Discussion S4. Detailed preparation process of PFSA membrane on the air/water interface.

For the highly packed PFSA membrane on the larger interface without defects, a homogenous PFSA monolayer must be made on the sufficient trough area. In this regard, 50 µL of the PFSA solution was spread with five separate steps using 10 µL for each step. The formed PFSA monolayer in each separate spreading step was compressed to *Π* = 54 mN/m by barriers, and expanded to the initial trough area, 243 cm^2 (**Figure S3a**). As each compression-decompression cycle proceeded, the hysteresis of *Π*-*A* isotherms of each cycle decreased, and *Π* at 54 mN/m was shifted to a larger trough area (**Figure S4a**). The hysteresis area of each cycle was integrated for a quantitative analysis of the *Π*-*A* isotherms. As shown in **Figure S4b**, the integrated hysteresis area decreases with increasing compression-decompression cycle number. In addition, the trough area at *Π* = 54 mN/m increases as the separate spreading steps were carried out (**Figure S4b**).

This means that the compactly packed PFSA monolayer, which may not re-spread on the interface, was formed without desorption from the interface. On the other hand, the maximum static compression modulus ($C_{s,\,max}^{-1}$) defined as $C_s^{-1} = -A(\partial \Pi/\partial A)_T$ was not changed, showing that the PFSA monolayer was still maintained without collapse (**Figure S4c**). From these results, it was confirmed that a homogenous PFSA monolayer with a densely packed structure was formed on the large trough area. After building the monolayer, the densely condensed PFSA monolayer with aligned side chains was finally prepared by compressing with a barrier speed of 5 mm/min. In the final compression step (com.), *Π-A* isotherm increases smoothly without changing the isotherm behavior, and the $C_{s,\,max}^{-1}$ exhibits the same value as in the previous cyclic steps (**Figure S4c, d**).

The deposition of PFSA monolayers on the surface of substrates was carried out using the Langmuir-Blodgett (LB) method, which can transfer the condensed monolayer in a layer-by-layer (LBL) manner.[11] In the up-stroke, hydrophilic side chains of the PFSA monolayer were contacted with the surface of substrate, and conversely, the hydrophobic backbones interact with the surface in the down-stroke. In accordance with cyclic up and down strokes, the PFSA monolayer on the air/water interface sequentially was transferred onto the substrate by LBL (**Figure S3b**). After the deposition steps, the ultrathin PFSA membranes on the substrate were dried at 80 °C for at least 16 hours.

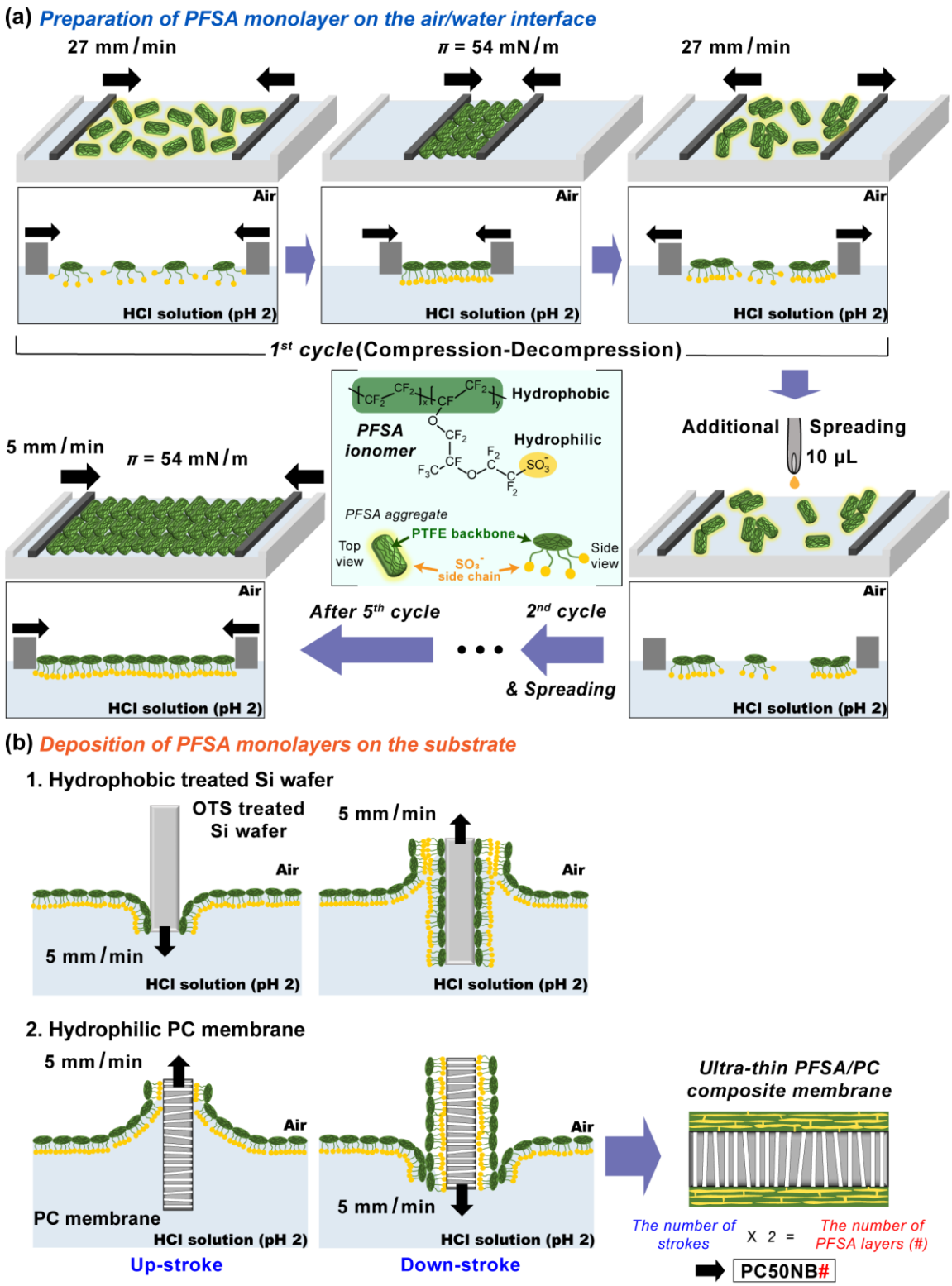

Figure S3. Schematic illustration of (a) preparation steps of ultrathin PFSA monolayer by separate addition method, and (b) deposition of PFSA monolayers on the substrates by Langmuir-Blodgett method; hydrophobic treated Si wafers and hydrophilic track-etched

polycarbonate (PC) membranes were used as substrates for structure analyses and VRFB membranes, respectively.

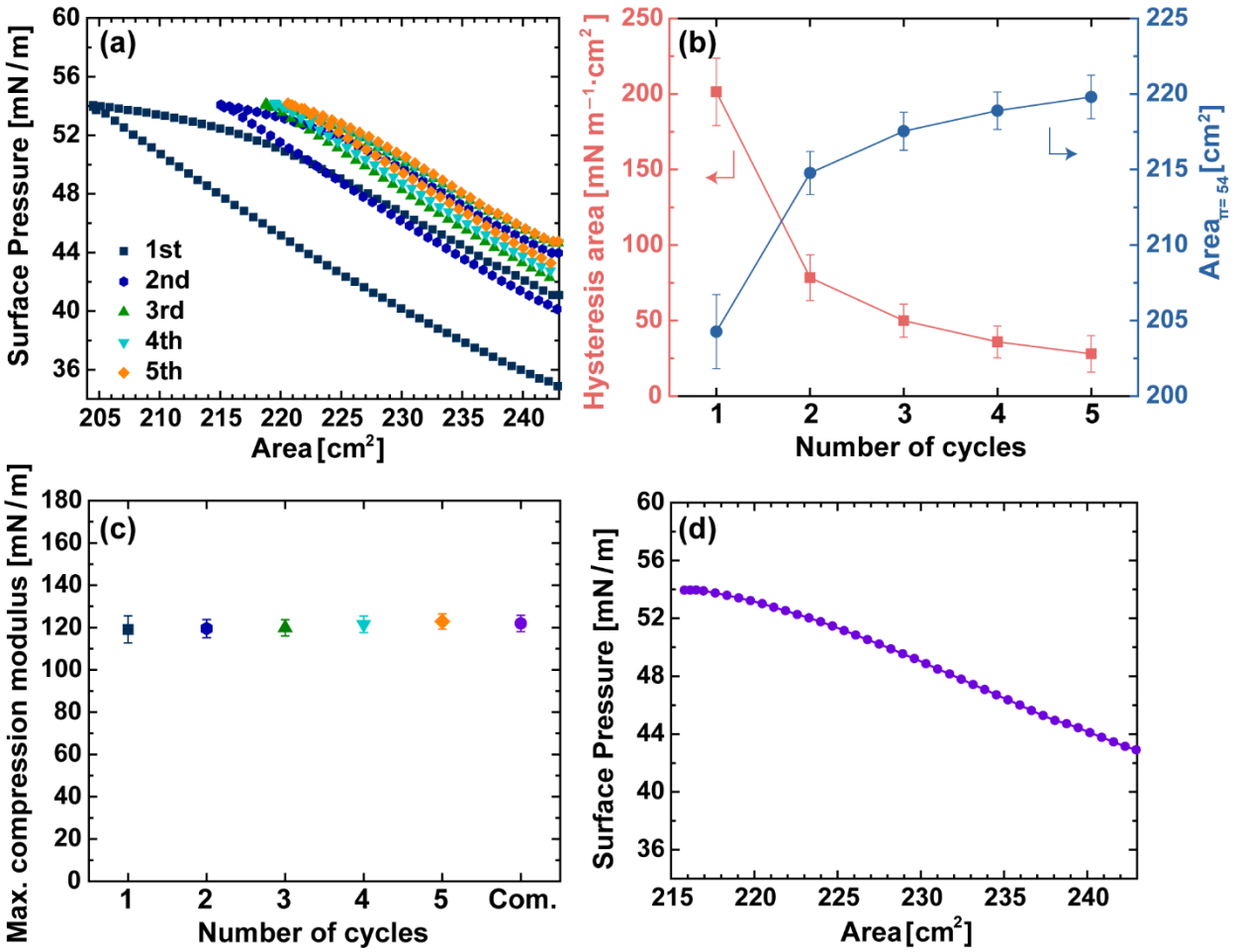

Figure S4. (a) *Π-A* isotherms of PFSA monolayer in each cycle, and (b) Quantitative analyses of *Π-A* isotherms; hysteresis area (red, left y-axis of graph) was calculated by integration between compression and expansion isotherm, and trough area at Π = 54 mN/m (blue, right y-axis of graph) was obtained from trough area in the each isotherm. (c) Maximum compression modulus ($C_{s,\,max}^{-1}$) of PFSA monolayer; it was derived from $C_s^{-1} = -A(\partial\Pi/\partial A)_T$. (d) *Π-A* isotherm in final compression step for the PFSA membrane.

Discussion S5. *Ex-situ* chemical stability of track-etched polycarbonate (PC) membrane

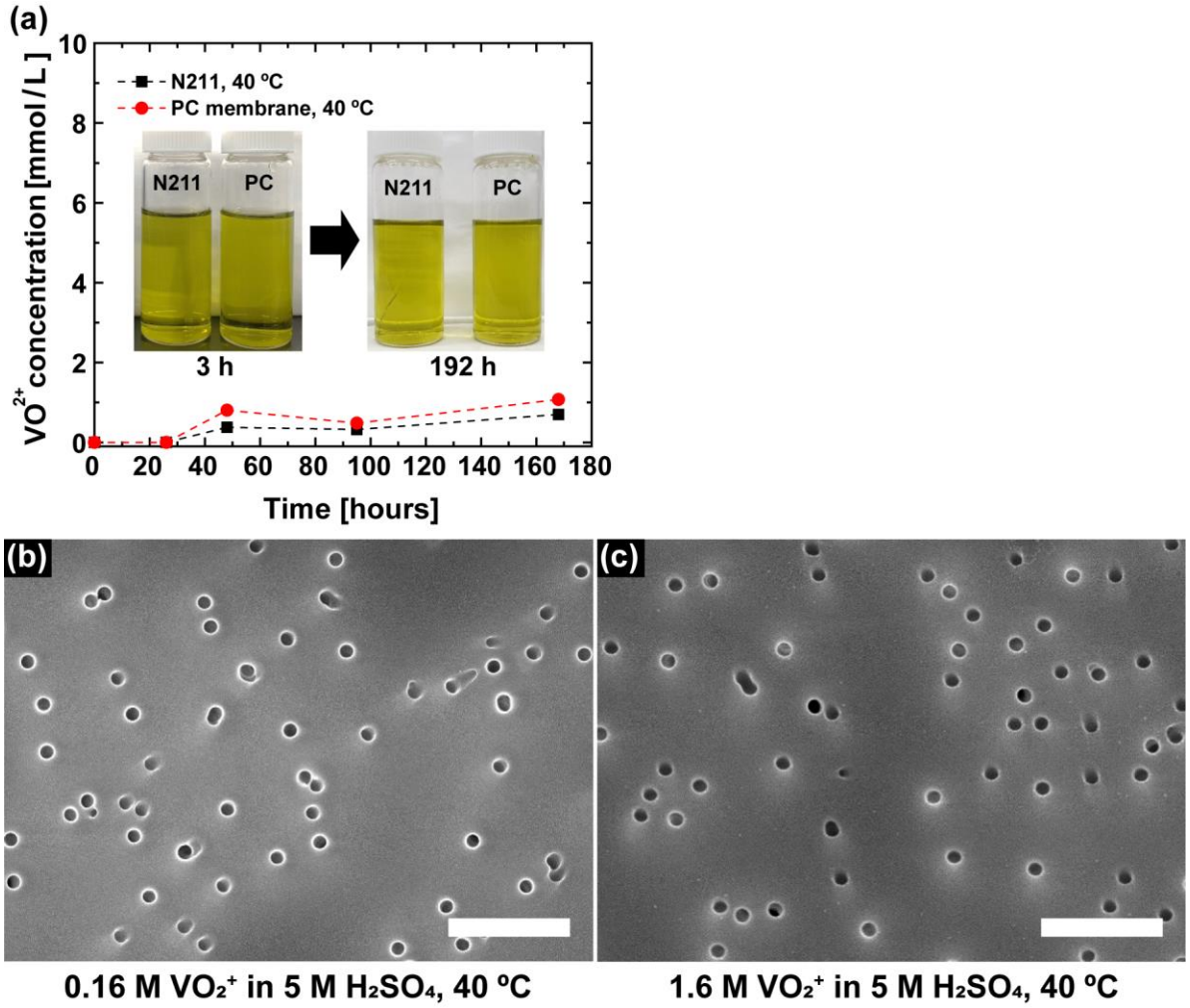

Figure S5. *Ex-situ* chemical stability test of N211 and PC membrane; (a) concentration change of VO^{2+} ions over time in 0.16 M of VO_2^+ in 5 M H_2SO_4 at 40 °C for 168 hours. The inserted images are the solutions of 0.16 M VO_2^+ in 5 M H_2SO_4 containing N211 and PC membrane after 3 and 192 hours. SEM images of PC membrane immersed in (b) 0.16 M of VO_2^+ in 5 M H_2SO_4 and (c) 1.6 M of VO_2^+ in 5 M H_2SO_4 at 40 °C for 192 hours (8 days), respectively. Scale bars are 1 μm.

The chemical stability of the PC membrane was evaluated using a VO_2^+ solution similar to the previously reported method.[12,13] A membrane (2.5 × 2.5 cm^2) and 20 mL of VO_2^+ solution were placed in the 25 mL vial. The immersion experiments were conducted at 40 °C for 7 days. For

comparison of the chemical stability, N211 was used as a control. The concentration change of VO^{2+} by reduction of VO_2^+ over time was measured using an UV–vis spectrometer (UV-2600, Shimadzu, Japan) at a maximum absorption peak of a 760 nm. As shown in **Figure S5a**, the PC membrane shows similar VO^{2+} concentration to N211 over time. In general, as the concentration of VO^{2+} ions increase by chemical degradation of membranes, the color of the VO_2^+ solution is changed from yellow to green (yellowish VO_2^+ mixed with blueish of VO^{2+}). However, the color of the VO_2^+ solution containing N211 and the PC membrane was not changed during 192 hours. In SEM images of the PC membrane immersed in 0.16 M of VO_2^+ in 5 M H_2SO_4 for 192 hours, no physical damage was observed (**Figure S5b**). In addition, the absence of chemical degradation was confirmed by the immersion test of the PC membrane in 1.6 M VO_2^+ in 5 M H_2SO_4, which is similar to the concentration of the VRFB electrolyte (**Figure S5c**).

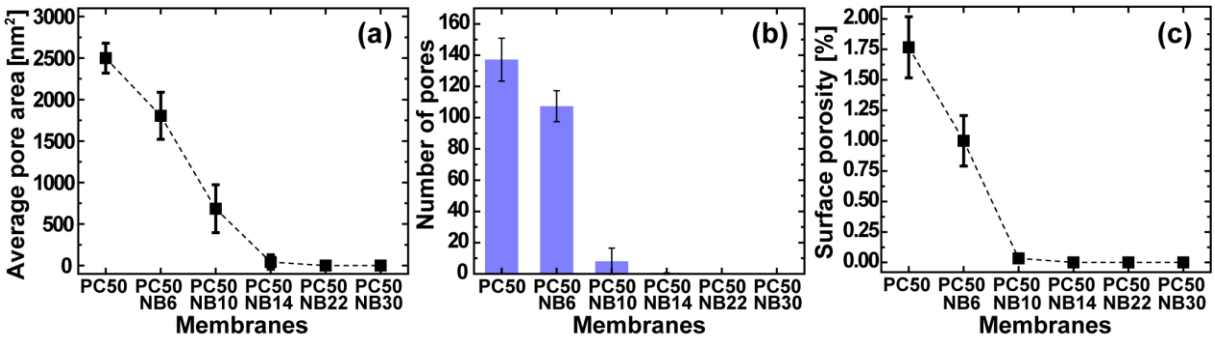

Figure S6. The results of quantitative analyses for pores of the membrane. (a) Average pore area of surface of the membrane. (b) Number of pores on the surface of the membrane. (c) Surface porosity of each membrane. As PFSA membranes were introduced on the surface of the PC membrane, the surface pores of the composite membrane became smaller and decreased. Above 22 layers of PFSA membrane, the surface pores of the composite membrane were completely covered.

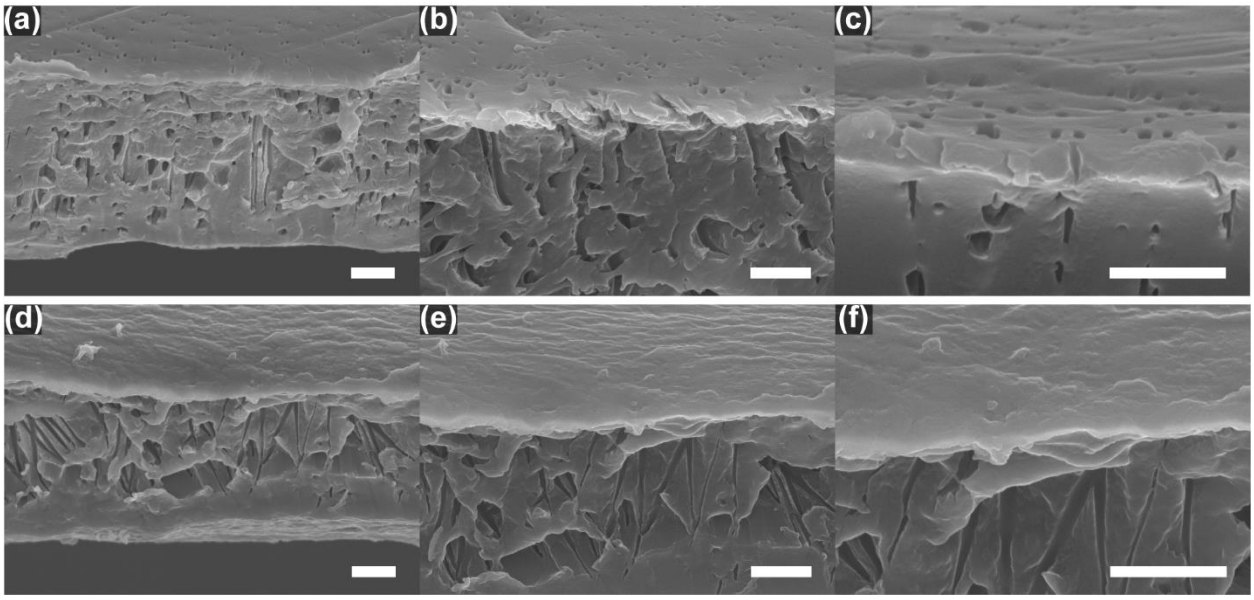

Figure S7. (a, b, c) The cross-sectional images of PC50 and (d, e, f) PC50NB30. The ultrathin PFSA layers cover the pores of PC50 without infiltration into the pores. Scale bars are 1 μm.

Discussion S6. Structural anisotropy analysis from GISAXS pattern: critical azimuthal angle.

To quantify the structural anisotropy, the critical azimuthal angle, ω^*, was calculated as reported in a literature.[14] The scattering intensity along ω was taken from the arc marked in **Figure S8a**. It was then integrated (I_Ω) as a function of ω, as delineated in **Equation S7**.

$$I_\Omega = \int_0^\Omega I(\omega) d\omega \ , \qquad \text{Equation S7}$$

where $I(\omega)$ is the scattering intensity as a function of ω. ω^* is then defined as the angle where the integrated value is half, as expressed in **Equation S8**.[14]

$$I_{\Omega}(\omega^{*})/I_{\Omega=90^{\circ}} = 0.5\ , \qquad \text{Equation S8}$$

where ω^{*} represents the degree of structural anisotropy. In addition, 45, 90, and 0 ° of ω^{*} correspond to random, perpendicular, and parallel orientation, respectively.

According to calculation with the scattering intensity along ω, the critical azimuth angle (ω^{*}) was very low ($\omega^{*}\approx3$ °), which means that the PFSA films stacked by the LB method are extremely aligned to be parallel to the substrate.

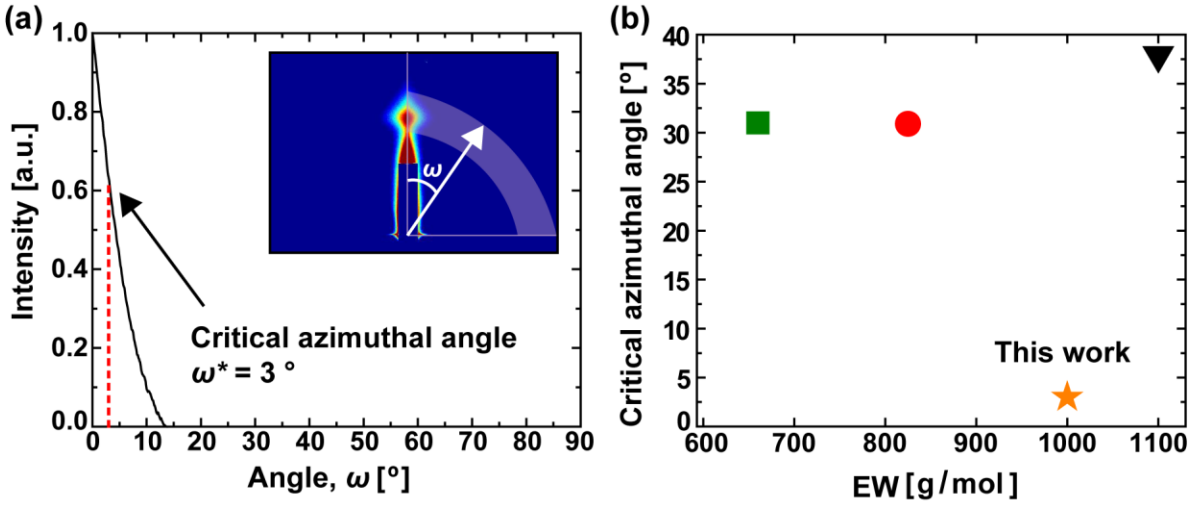

Figure S8. (a) Intensity profile along the azimuthal angle extracted following the marked arc as shown in the inset image. From integration of the profile of the scattering intensity along the angle, the critical azimuth angle (ω^{*}) was calculated using **Equation S8**. (b) Comparison of the critical azimuth angle of ultrathin PFSA film (yellow star) with the results from Kusoglu et al. (reproduced with the permission from ref. 14. Copyright 2016 John Wiley and Sons, PFSA thin film of 50 nm and 100 nm fabricated by spin coating: green square, red circle, and black inverted triangle indicate the spin-coated thin films with the EW of 660, 825, and 1100, respectively). The degree of anisotropy of ultrathin PFSA film was analyzed with the GISAXS pattern of PFSA-N48. For spin-coated PFSA thin films, the critical azimuthal angle decreases at lower EW because the film has more anisotropic orientation owing to enhancing interaction between ionic

moieties of PFSA film and the substrate. For the ultrathin PFSA film fabricated by the Langmuir-Blodgett method, the critical azimuth angle was much lower than that of spin-coated thin films even though EW is higher.

Discussion S7. Structural anisotropy analysis from GISAXS pattern: Herman's orientation factor.

Herman's orientation factor, *f*, which is another quantification factor for the degree of orientation, was evaluated to verify the highly ordered structure of PFSA membranes. From the intensity profile along the azimuthal angle (**Figure S8a**), *f* was calculated from **Equation S9**.

$$f = \frac{3<\cos^2\omega>-1}{2}. \qquad \text{Equation S9}$$

The average of $\cos^2\omega$ was evaluated between $\omega = 0$ and $\pi/2$ using **Equation S10**.

$$<\cos^2\omega> = \frac{\int_0^{\pi/2} I(\omega)\sin\omega\,\cos^2\omega\,d\omega}{\int_0^{\pi/2} I(\omega)\sin\omega\,d\omega}. \qquad \text{Equation S10}$$

The value of *f* is equal to 0, 1, or −0.5 indicating an isotropy system, perfect parallel orientation, and perfectly vertical orientation to the plane of a substrate, respectively.

That is, the high intensity at a small azimuthal angle in the profile result means that the polymer nanostructure is almost perfectly aligned in the parallel direction. Previously, a study of PFSA thin films revealed that spin-coated Nafion thin films show parallel orientations to a gold

substrate using variable angle spectroscopic ellipsometry (VASE) and GISAXS. *f* for a 17 nm thick film was 0.45.[15] For the PFSA monolayers deposited on PC50 by the LB method, interestingly, *f* was 0.98, and this value was much higher than that of the PFSA film coated on the metal substrate.

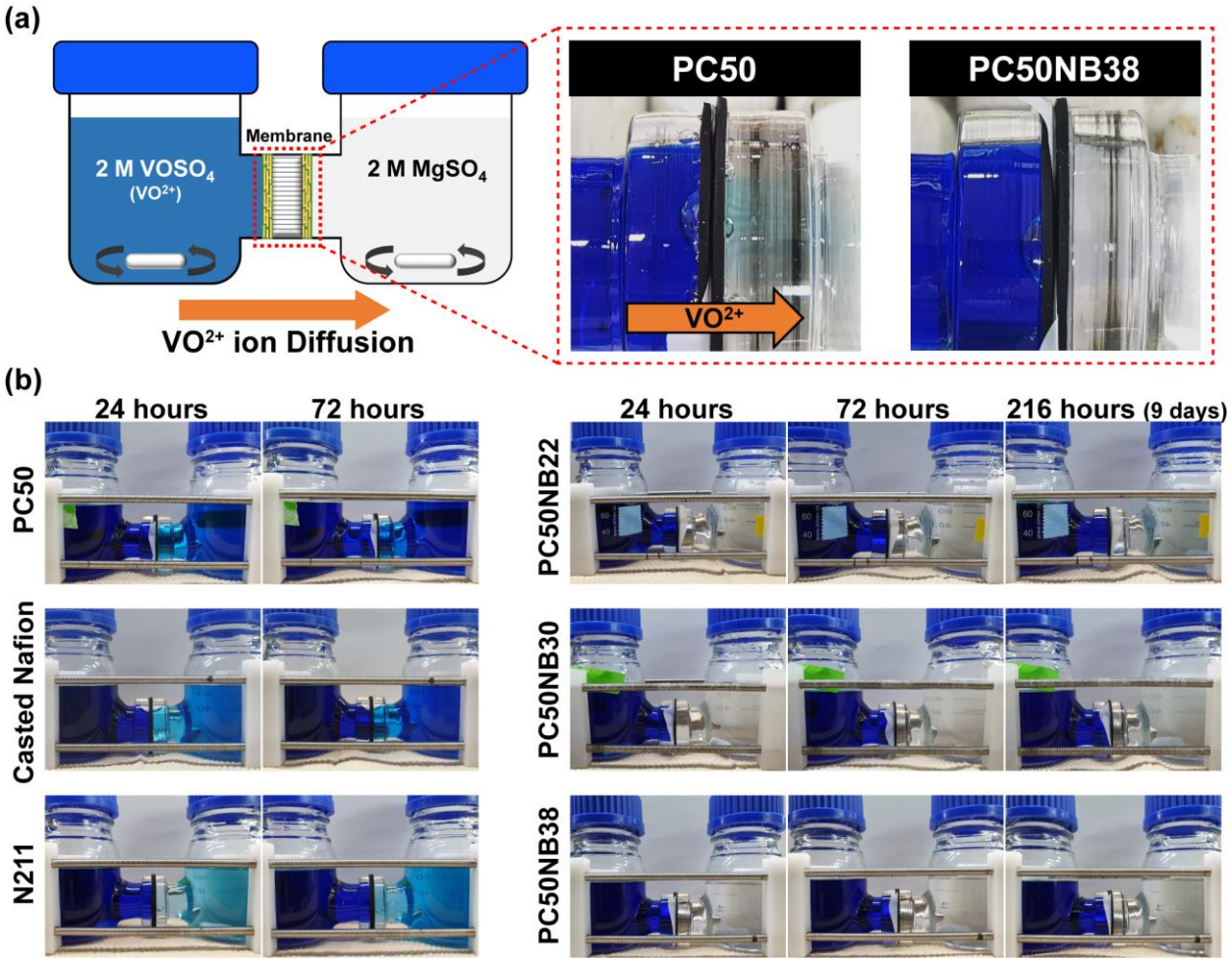

Figure S9. (a) Schematic illustration of a diffusion cell for VO^{2+} ion permeation through a membrane. Immediately after starting the experiments, through pristine PC membrane (PC50), VO^{2+} diffused to $MgSO_4$ solution under the concentration gradient, but not through the ultrathin PFSA/PC composite membrane. (b) Images of diffusion cell over time. For the ultrathin PFSA/PC composite membrane, the color of the $MgSO_4$ solution was little changed even after 216 hours (9 days) compared to N211, casted Nafion membrane, and PC50.

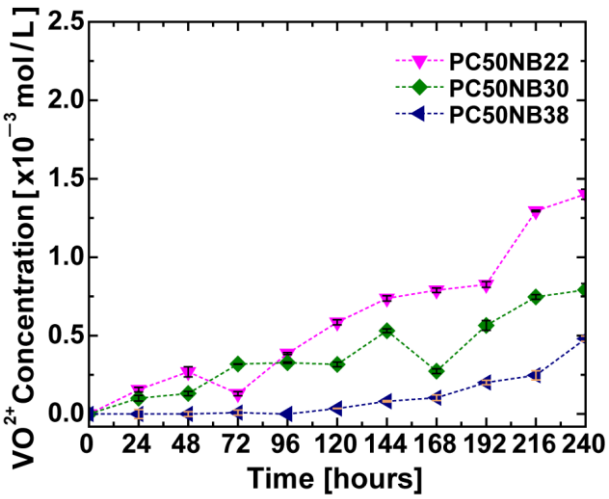

Figure S10. Concentration of permeated VO^{2+} ion across the ultrathin PFSA/PC composite membranes. The permeation rate decreases as the number of deposited PFSA monolayers increases.

Discussion S8. Series model for permeation and resistance of ultrathin PFSA membrane.

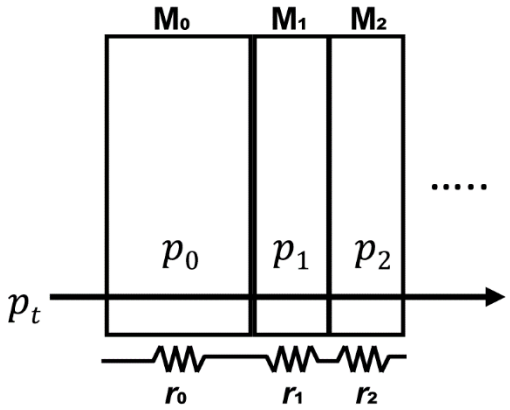

Figure S11. Series model for permeance and resistance of a layered composite membrane.

An ultrathin PFSA/PC composite membrane consists of a PC membrane and multilayers of 1.4 nm PFSA monolayers. Thus, it was simply assumed to be membranes connected in series (**Figure S11**). As shown in **Figure S6**, when more than 22 layers of the PFSA film was

deposited, the pores of the PC film were completely blocked, but for simple estimation, it was assumed that all the deposited layers cover the pores without any damage.

The VO^{2+} permeability (P) of the PFSA membrane obtained from the permeance (p) of the composite membrane. As shown in **Figure S11**, the total permeance of membranes in series is calculated using **Equation S11** below.

$$1/p_t = 1/p_0 + 1/p_1 + 1/p_2 + \dots , \qquad \text{Equation S11}$$

where p_t is the total permeance of a composite membrane, and p_0, p_1, and p_2 are permeances of each layer. For the PFSA/PC composite membrane, since the identical PFSA layers are stacked on the PC membrane, **Equation S11** can be simplified to **Equation S12**,

$$1/p_{PC50NBn} = 1/p_{PC50} + n/p_{PFSA\text{-}N1} , \qquad \text{Equation S12}$$

where n is the number of PFSA monolayers deposited on the PC membrane, $p_{PC50NBn}$ is the permeance of the composite membrane containing n PFSA monolayers, p_{PC50} is the permeance of the PC membrane, and $p_{PFSA\text{-}N1}$ is the permeance of the PFSA monolayer. $p_{PC50NBn}$ of the composite membranes and p_{PC50} are displayed in **Table S1**.

Lastly, from the thickness of PFSA-N1 ($L_{PFSA\text{-}N1}$ =1.4 nm) and $p_{PFSA\text{-}N1}$ (**Equation S12)**, the permeability of one PFSA membrane ($P_{PFSA\text{-}N1}$) can be estimated using **Equation S13**, and the results are shown in **Table 1** in the main text.

$$P_{\text{PFSA-N1}} = L_{\text{PFSA-N1}} \times p_{\text{PFSA-N1}} . \qquad \text{Equation S13}$$

In order to estimate the proton conductivity ($\sigma_{\text{PFSA-N1}}$) of the PFSA monolayer, the resistance of the PFSA membrane was calculated using **Equation S15** derived from total resistance of the membrane (**Equation S14**).

$$r_t\,[\Omega] = r_0 + r_1 + r_2 + \dots , \qquad \text{Equation S14}$$

where r_t is the total resistance of the membrane, and r_0, r_1, and r_2 are the resistances of each layer.

$$r_{\text{PC50NB}n} = r_{\text{PC50}} + n \times r_{\text{PFSA-N1}} , \qquad \text{Equation S15}$$

where r_{PC50NBn} is the resistance of the composite membrane containing n PFSA monolayers, r_{PC50} is the resistance of the PC membrane, and $r_{\text{PFSA-N1}}$ is the resistance of the PFSA monolayer. The r_{PC50NBn} of the composite membrane and r_{PC50} are displayed in **Table S1**. Using **Equation S5** with $R_{\text{PFSA-N1}}$ ($R_{\text{PFSA-N1}} = r_{\text{PFSA-N1}} \times A$, where A is active area), $\sigma_{\text{PFSA-N1}}$ can be obtained, and the results are shown in **Table 1**.

Table S1. Permeance and resistance of membranes.

Membrane	The number of PFSA layers	Permeance [m/s][a)]	Resistance [Ω][b)]
N211	–	1.49×10^{-8}	1.40 ± 0.01
Casted Nafion	–	4.90×10^{-8}	1.26 ± 0.01
PC50	–	2.79×10^{-7}	1.20 ± 0.01
PC50NB22	22	2.30×10^{-10}	1.63 ± 0.03
PC50NB30	30	1.43×10^{-10}	1.68 ± 0.03
PC50NB38	38	3.71×10^{-11}	1.75 ± 0.02

[a)]The value of permeance (p) was calculated by **Equation S2**; [b)]The resistance (r) of membrane was obtained by $r = r_2 - r_1$, where r_2 and r_1 are the resistance with and without membrane, respectively.

Discussion S9. Estimation of tortuosity and ion channel size effect of ultrathin PFSA membrane.

Mobile ions are transported through the ion conducting channels of the PFSA membrane. We estimated the tortuosity of the ultrathin PFSA layers on PC50, and N211, and explored the effect of ion conducting channel size on the ion selectivity. In general, the ions transfer through a PFSA membrane via a vehicle mechanism, but for protons, a hopping mechanism is additionally contributed to the proton conduction.[9,16] Neglecting the hopping mechanism, the effective mobility (u_{eff}) in a membrane is proportional to $u_{\text{eff}} \sim \theta(1-\lambda)^2/\tau$, where θ is the ion conducting channel volume fraction, λ is the ratio of ion diameter (d_{ion}) to the conducting path diameter (d_{path}), $\lambda = d_{\text{ion}}/d_{\text{path}}$, and τ is the tortuosity.[17] The effective channel diameter for ion transport by the vehicle mechanism was assumed to be the space of the hydrophilic channel excluding the side-chain length (~1 nm)[18,19] in the membrane (the effective channel diameter : ~3 nm for

general PFSA membrane and ~0.85 nm for ultrathin PFSA membrane). For a mobile ion with the hydrated ion diameters (~0.3 nm for proton,[20] and ~0.6 nm for vanadium ion[21]), considering λ of N211 (λ_{N211}) and ultrathin PFSA membrane ($\lambda_{ultrathin\ PFSA}$) by $(1-\lambda_{N211})^2/(1-\lambda_{ultrathin\ PFSA})^2 \sim 7$, the relation between the effective mobility of N211 and the ultrathin PFSA membrane can be reproduced as $u_{eff,N211}/u_{eff,ultrathin\ PFSA} \sim P_{N211}/P_{ultrathin\ PFSA} = P_{N211}/P_{PFSA\text{-}N1} \sim 7 \times (\tau_{ultrathin\ PFSA}/\tau_{N211})$ under the assumption that the partitioning of a mobile ion is similar for all systems. From the P of each membrane, it is confirmed that the ultrathin PFSA membrane has much higher tortuosity than N211 ($\tau_{ultrathin\ PFSA} \sim 10^4 \times \tau_{N211}$).

For ion channel size effects on ion transport, we estimated the relative difference in each u_{eff} of the proton and vanadium ion in the ion channels of the membranes. In other words, the relative difference ($v = u_{proton}/u_{vanadium}$) of proton and vanadium ion moving in the channel is related with $v \sim (1 - \lambda_p)^2/(1 - \lambda_v)^2$, where $\lambda_p = d_{proton}/d_{path}$, and $\lambda_v = d_{vanadium}/d_{path}$. From the hydrated ion diameters of proton and vanadium ion and the effective ion channels of each membrane, v was obtained as $v_{N211} = 1.3$ and $v_{PFSA/PC} = 4.8$, indicating that the reduced channel size makes more difference in the ion transport in the channel.

From these results, it is confirmed that the highly ordered hydrophilic channel of ultrathin PFSA membrane has higher tortuosity than N211, and its reduced channel size induces a great impact on ion transport rate of proton and vanadium ion. We thus could conclude that the higher ion selectivity of the ultrathin PFSA membrane originates from its nanomorphology.

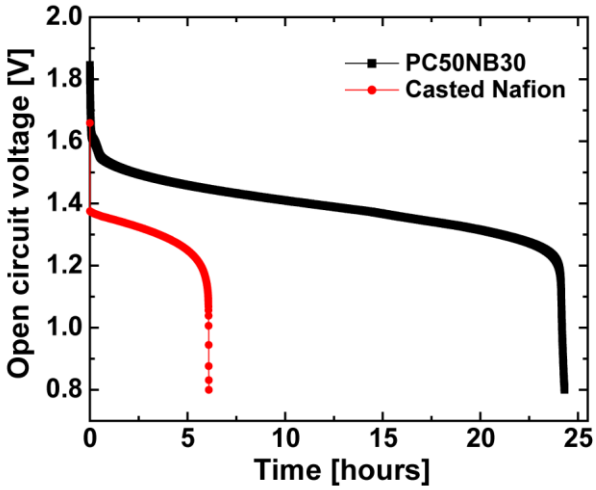

Figure S12. Open circuit voltage of PC50NB30 and Casted Nafion.

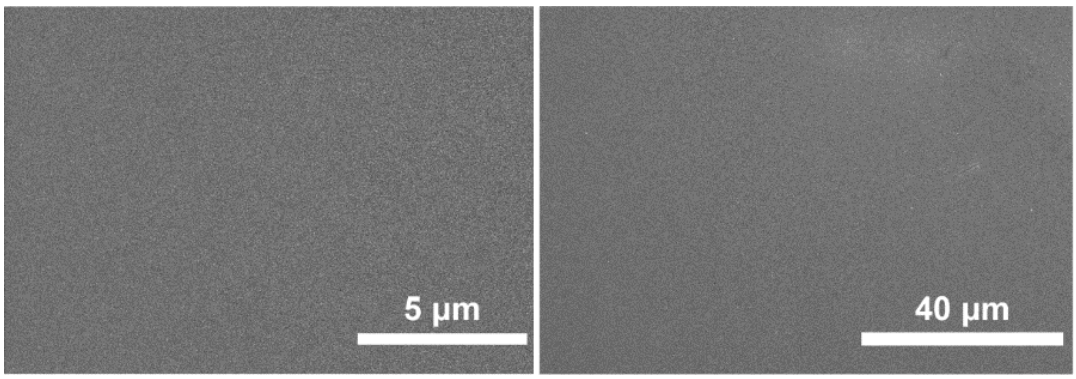

Figure S13. SEM images of PC50NB30 after the rate performance test at 40, 60, 80, 100, 150, and 200 mA/cm^2.

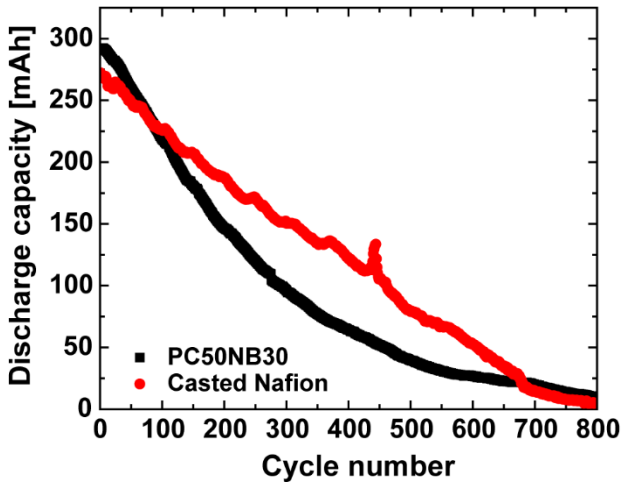

Figure S14. Discharge capacity of PC50NB30 and CN during the long-term cycling test at 200 mA/cm^2.

REFERENCES

(1) Bertoncello, P.; Peruffo, M.; Li, F.; Unwin, P. R. Functional Electrochemically-Active Ultra-Thin Nafion Films. *Colloids Surfaces A Physicochem. Eng. Asp.* **2008**, *321* (1–3), 222–226.

(2) Bertoncello, P.; Notargiacomo, A.; Nicolini, C. Langmuir−Schaefer Films of Nafion with Incorporated TiO 2 Nanoparticles . *Langmuir* **2005**, *21* (1), 172–177.

(3) Kim, B. Q.; Chae, J.; Kim, J. Q.; Kim, K.; Choi, S. Q. Interfacial Shear Rheology of Perfluorosulfonic Acid Ionomer Monolayers at the Air/Water Interface. *J. Rheol.* **2019**, *63* (6), 947–959.

(4) Saito, M.; Arimura, N.; Hayamizu, K.; Okada, T. Mechanisms of Ion and Water Transport in Perfluorosulfonated Ionomer Membranes for Fuel Cells. *J. Phys. Chem. B* **2004**, *108* (41), 16064–16070.

(5) Moukheiber, E.; De Moor, G.; Flandin, L.; Bas, C. Investigation of Ionomer Structure through Its Dependence on Ion Exchange Capacity (IEC). *J. Membr. Sci.* **2012**, *389*, 294–304.

(6) Bertoncello, P.; Ram, M. K.; Notargiacomo, A.; Ugo, P.; Nicolini, C. Fabrication and Physico-Chemical Properties of Nafion Langmuir-Schaefer Films. *Phys. Chem. Chem. Phys.* **2002**, *4*, 4036–4043.

(7) Ugo, P.; Bertoncello, P.; Vezzà, F. Langmuir-Blodgett Films of Different Ionomeric Polymers Deposited on Electrode Surfaces. *Electrochim. Acta* **2004**, *49*, 3785–3793.

(8) Shi, S.; Weber, A. Z.; Kusoglu, A. Structure-Transport Relationship of Perfluorosulfonic-Acid Membranes in Different Cationic Forms. *Electrochim. Acta* **2016**, *220*, 517–528.

(9) Peng, J.; Lou, K.; Goenaga, G.; Zawodzinski, T. Transport Properties of Perfluorosulfonate Membranes Ion Exchanged with Cations. *ACS Appl. Mater. Interfaces* **2018**, *10* (44), 38418–38430.

(10) Madivala, B.; Fransaer, J.; Vermant, J. Self-Assembly and Rheology of Ellipsoidal Particles at Interfaces. *Langmuir* **2009**, *25* (5), 2718–2728.

(11) Ariga, K.; Yamauchi, Y.; Mori, T.; Hill, J. P. 25th Anniversary Article: What Can Be Done with the Langmuir-Blodgett Method? Recent Developments and Its Critical Role in Materials Science. *Adv. Mater.* **2013**, *25* (45), 6477–6512.

(12) Sukkar, T.; Skyllas-Kazacos, M. Membrane Stability Studies for Vanadium Redox Cell Applications. *J. Appl. Electrochem.* **2004**, *34* (2), 137–145.

(13) Kim, S.; Tighe, T. B.; Schwenzer, B.; Yan, J.; Zhang, J.; Liu, J.; Yang, Z.; Hickner, M. A. Chemical and Mechanical Degradation of Sulfonated Poly(Sulfone) Membranes in Vanadium Redox Flow Batteries. *J. Appl. Electrochem.* **2011**, *41* (10), 1201–1213.

(14) Kusoglu, A.; Dursch, T. J.; Weber, A. Z. Nanostructure/Swelling Relationships of Bulk and Thin-Film PFSA Ionomers. *Adv. Funct. Mater.* **2016**, *26* (27), 4961–4975.

(15) Kushner, D. I.; Kusoglu, A.; Podraza, N. J.; Hickner, M. A. Substrate-Dependent Molecular and Nanostructural Orientation of Nafion Thin Films. *Adv. Funct. Mater.* **2019**, *29* (37), 1902699.

(16) Vijayakumar, M.; Luo, Q.; Lloyd, R.; Nie, Z.; Wei, X.; Li, B.; Sprenkle, V.; Londono, J. D.; Unlu, M.; Wang, W. Tuning the Perfluorosulfonic Acid Membrane Morphology for Vanadium Redox-Flow Batteries. *ACS Appl. Mater. Interfaces* **2016**, *8* (50), 34327–34334.

(17) Satterfield, C. N.; Colton, C. K.; Pitcher, W. H. Restricted Diffusion in Liquids within Fine Pores. *AIChE J.* **1973**, *19* (3), 628–635.

(18) Paul, D. K.; Karan, K.; Docoslis, A.; Giorgi, J. B.; Pearce, J. Characteristics of Self-Assembled Ultrathin Nafion Films. *Macromolecules* **2013**, *46* (9), 3461–3475.

(19) Karan, K. Interesting Facets of Surface, Interfacial, and Bulk Characteristics of Perfluorinated Ionomer Films. *Langmuir* **2019**, *35* (42), 13489–13520.

(20) Nightingale, E. R. Phenomenological Theory of Ion Solvation. Effective Radii of Hydrated Ions. *J. Phys. Chem.* **1959**, *63* (9), 1381–1387.

(21) Oriji, G.; Katayama, Y.; Miura, T. Investigations on V(IV)/V(V) and V(II)/V(III) Redox Reactions by Various Electrochemical Methods. *J. Power Sources* **2005**, *139* (1–2), 321–324.